Journal of Environmental Chemical Engineering 9 (2021) 104809

Contents lists available at ScienceDirect

Journal of Environmental Chemical Engineering

journal homepage: www.elsevier.com/locate/jece

Photocatalytic generation of gas phase reactive oxygen species from adsorbed water: Remote action and electrochemical detection

Xinwei Sun, Kaiqi Xu, Athanasios Chatzitakis *, Truls Norby *

Centre for Materials Science and Nanotechnology, Department of Chemistry, University of Oslo, FERMiO, Gaustadalléen 21, NO-0349 Oslo, Norway

ARTICLE INFO

Editor: Dr. G. Palmisano

Keywords:
Solid-state photocatalysis
Gas phase
Titanium dioxide
Reactive oxygen species
Air purification

ABSTRACT

The improvement of indoor environments is of great importance as it can significantly improve human health, comfort and productivity. Herein, different forms of TiO_2 nanorods were used as the photocatalyst for generation of reactive oxygen species (ROS) in a gas phase photoreactor under controlled humidity. Several parameters were investigated by monitoring the remote decolourisation of Methylene Blue (MB) embedded in a Nafion film. A decolourisation of 26% under 80% relative humidity was observed when the MB film was 0.5 cm away from the photocatalyst. The length and ratio of light/dark intervals have major impacts on the efficiency of the gas phase photocatalytic process, which we link to the amount of water adsorbed on the photocatalyst, as the source for hydroxyl radicals. Furthermore, the photocatalytic production of ROS was quantified through a polyaniline electrochemical sensor and a rate of $1 \cdot 10^{12}$ of ROS molecules s^{-1} was estimated. This study contributes to the efficacy of the gas phase photocatalytic method in air decontamination, for the development of efficient air cleaning devices.

1. Introduction

Indoor air is often more polluted than outdoors, as it contains not only the outdoor pollutants, but also pollutants from other sources, such as household and construction materials [1,2]. As people spend most of their time indoors, there is an increasing need in further investment in the air quality, which has a major impact on human health, as well as productivity and comfort [3,4]. Common diseases due to poor indoor air quality are related to respiratory problems, such as asthma, allergies, sick building syndrome (SBS) and in extreme cases even cancer [5,6]. According to Verbruggen [2], the improvement of the indoor air quality can lead to a gain of 37–200 billion USD by reducing the aforementioned diseases.

In practice, source control is often unrealistic. Ventilators and air purifiers based on filters and absorbents may transfer the problem from the air to handling the filters. A potential solution is through photocatalytic oxidation (PCO), as vast research shows that PCO can convert a wide range of gaseous pollutants, such as volatile organic compounds (VOCs), including aromatics, esters, alcohols, alkanes etc. [4,7,8], as well as bacteria and other microorganisms [9] into nontoxic carbon dioxide and water. The effectiveness of PCO as an advanced oxidation process (AOP) relies mainly on the formation of hydroxyl radicals, $OH^{\bullet}$ ($E^0_{OH\bullet/H2O} = +2.8$ V vs. NHE), which are among the strongest gaseous oxidising species [10–13]. Titanium dioxide (TiO_2) is one of the most studied and appropriate photocatalysts for PCO due to its low-cost, earth abundancy, chemical stability, non-toxicity and high oxidation power [6,14]. Nevertheless, TiO_2 has two main disadvantages, one being its wide band gap (3.0–3.2 eV, activated only by UV light) and the other is its deactivation due to adsorption of air contaminants, e.g. toluene [15]. Moreover, the role of water vapour is not clear as there are contradicting results, showing that water vapour either improves the photocatalytic degradation process [16–18] or inhibits it [19–22].

In our work, we chose a different approach, which is based on the concept of hydroxyl radical ($OH^{\bullet}$) generators, such as the commercial ODOROX® air purifier [23]. This device generates $OH^{\bullet}$ in the gas-phase by direct photolysis of the humidity of ambient air using UVC radiation from a mercury lamp to eliminate bacteria, trace gases, mould and VOCs in indoor environment. The purified air is redelivered back to the environment along with $OH^{\bullet}$, which can further oxidise airborne contaminants. However, it is uncertain how many $OH^{\bullet}$ are actually released from this device, hence how big effect they have on the air quality. The direct measurement of the $OH^{\bullet}$ concentration is also very challenging [24], especially in gas phase photocatalytic systems. It should also be noted that to distinguish in the gas phase between hydroxyl radicals and

* Corresponding authors.
E-mail addresses: a.e.chatzitakis@smn.uio.no (A. Chatzitakis), truls.norby@kjemi.uio.no (T. Norby).

https://doi.org/10.1016/j.jece.2020.104809
Received 7 September 2020; Received in revised form 27 October 2020; Accepted 9 November 2020
Available online 22 November 2020

other reactive oxygen species (ROS) such as superoxide anion radicals ($O_2^{\bullet -}$), hydrogen peroxide (H_2O_2) and singlet oxygen ($^1O_2$) is challenging, as delicate gas phase fluorescence experiments (e.g. laser induced fluorescence – LIF) are necessary. Although hydroxyl radicals are expected to be one of the main photocatalytic products, we will still refer to ROS as the product of the photocatalytic experiments in general. Finally, the distance that ROS can travel before they react with other gas molecules is also a critical parameter of the efficiency of such an air purifying device. Some important chemical reactions in this respect are listed (Eqs. (1–7))

$$OH^{\bullet} + OH^{\bullet} \rightarrow H_2O_2 \quad (1)$$

$$2OH^{\bullet} + H_2 \rightarrow 2H_2O \quad (2)$$

$$OH^{\bullet} + CO + O_2 \rightarrow HO_2^{\bullet} + CO_2 \quad (3)$$

$$OH^{\bullet} + CH_4 + O_2 \rightarrow CH_3O_2^{\bullet} + H_2O \quad (4)$$

$$OH^{\bullet} + H_2O_2 \rightarrow HO_2^{\bullet} + H_2O \quad (5)$$

$$(O_2)_{ads} + e^- \rightarrow (O_2^{\bullet -})_{ads} \quad (6)$$

$$(O_2^{\bullet -})_{ads} + h^+ \rightarrow (^1O_2) \quad (7)$$

Our work is divided into two tasks. The first is related to the effect of the distance that ROS can travel and degrade pollutants. A simple approach is followed and is based on a model pollutant, the Methylene Blue (MB) dye, which is embedded in a Nafion® film. This is used as a colourimetric indicator for the indirect detection of ROS as well as the distance that they can cover. The MB indicator is placed in proximity of the surface of the photocatalyst, which is TiO_2 in the form of nanorods. The efficiency of the photocatalyst for decolourisation of the MB film at two distances is studied. Moreover, the kinetic behaviour of the reaction is analysed.

In the second task, the best performing parameters found previously are chosen and an attempt to estimate the ROS concentration is made. For this purpose, a microchip sensor based on polyaniline (PANI) is developed and used to monitor the real-time photo-generation of ROS [25,26]. It should be noted though that the specific sensor was developed for the detection of hydroxyl radicals with the Fenton reaction, therefore in this case we are referring to hydroxyl radicals and a one electron oxidation reaction. By the charge integration between light-on and light-off periods, we were able to estimate the amount of hydroxyl radicals produced by the photocatalyst under certain conditions.

2. Experimental

2.1. Chemicals and materials

Fluorine-doped tin oxide (FTO), titanium isopropoxide (TTIP, 97%), hydrochloric acid (HCl, 37%), urea ($CO(NH2)_2$, ≥ 99.5%), isopropanol, acetone, methylene blue (MB, 98.5%), Nafion® perfluorinated resin solution 5 wt% in lower aliphatic alcohols and 15–20% water (Nafion5), sulphuric acid (≥ 97.5%), Aniline (ACS reagent, ≥ 99.5 wt%), iron (II) sulphate heptahydrate (≥ 99%), hydrogen peroxide (30% wt in H_2O, with stabiliser) were all of analytical grade from Sigma-Aldrich. Potassium dihydrogen phosphate (ACS, 99%) and potassium hydrogen phosphate (ACS, 98%) were purchased from Alfa Aesar. All chemicals were used without further purification. Interdigitated gold electrodes (IDE) were purchased from DropSens and consisted of 500 fingers with a width of 5 μm, a length of 6760 μm each and 5 μm gaps. Regular compressed air was obtained from Praxair. All solutions were prepared using deionized water (DI water) with 18.2 MΩ cm resistance.

2.2. TiO_2 nanorods preparation

TiO_2 of different morphologies were grown on FTO substrates via a previously reported hydrothermal method [27]. Prior to synthesis, all FTO were cut in pieces of 1.5 × 1.5 cm, in order to obtain the same nominal surface area for the different photocatalytic films, and were ultrasonically cleaned for 60 min in a 1:1:1 vol ratio mixture of DI water, acetone and isopropanol. All the experimental conditions are summarised in Table 1. Four morphologies of TiO_2 were obtained, which are (a) TiO_2 nanorods (TiO_2 NRs), (b) dense-packed TiO_2 nanorods (DP TiO_2 NRs), (c) dense-packed TiO_2 nanoflowers (DP TiO_2 NFs) and (d) dense-packed 1% N-doped TiO_2 nanorods (DP 1% N-TiO_2 NRs). The total volume of the autoclave was 30 mL and each hydrothermal reaction for the growth of the respective morphology was done at 150 °C. The time for each morphology is denoted in Table 1. After completion of the reaction, the autoclave was cooled down under flowing water for 15 min

It was suggested that the growth of TiO_2 NRs on FTO substrate was favoured when equal amounts of DI water and HCl were used. Moreover, the placement of the FTO in the autoclave has an influence on the morphology of the nanorods film. When the FTO is placed horizontally with respect to the base of the autoclave and the conducting side facing down, the nanoflowers morphology is obtained. Accordingly, when the FTO is placed vertically with the conducting side facing towards the wall of the autoclave, the aligned nanorods morphology is obtained. The experimental setup is schematically depicted in Fig. S1.

2.3. Preparation of the colourimetric indicator

0.3 g MB was dissolved in 0.5 L of DI water to get a MB solution with concentration of 0.6 g L^{-1}. Afterwards, 2 mL of the MB solution were mixed with 1 mL of the Nafion5 solution. The colourimetric MB indicator is prepared by evenly spreading the mixture on a masked glass substrate, which is then dried in air. Finally, the masking tape was removed and a rectangular MB film was obtained (see Fig. S2).

2.4. Preparation of the PANI sensor

The PANI film was electrodeposited by potentiostatic pulse electrodeposition in a three-electrode setup, which consists of the IDE as the working electrode, a platinum foil as the counter electrode and a saturated calomel electrode (SCE) as the reference electrode. The IDE had two connection tracks, made of Au with 20 at% Ti alloy, on a glass substrate, as illustrated in Fig. S3. According to previous studies, the electrodeposition was carried out in an aqueous solution prepared by carefully mixing 0.2 M aniline monomer precursor in 0.5 M H_2SO_4 aqueous solution as the electrolyte [28,29]. Before electrodeposition, the IDE was ultrasonically cleaned in a mixture of acetone and isopropanol for 5 min and then rinsed with DI water, followed by 20 CV cycles (1 V s^{-1}) between − 1 V and 2.4 V vs. SCE in 0.5 M H_2SO_4. The PANI films were produced by a pulse potentiostatic method (PPM) with an anodic potential of 0.806 V vs. SCE and a cathodic potential of 0.256 V vs. SCE. The duration at each potential was 0.5 s, while the total electrodeposition time was 500 s. When the deposition process was completed, a few drops of HCl of pH 2 were added on the active sensing

Table 1
Summary of experimental conditions and results at 150 °C on FTO substrate.

DI water (mL)	HCl (37%) (mL)	TTIP (97%) (mL)	Urea from a 0.03 g L^{-1} solution (mL)	Time (h)	Morphology
10	10	0.5	0	2.5	TiO_2 NRs
10	10	0.5	0	4	DP TiO_2 NRs
10	10	0.5	0	4	DP TiO_2 NFs
9.65	10	0.5	0.35	4	DP 1% N-TiO_2 NRs

area on the IDE, and then dried in ambient air. The pulsed electrodeposition steps are schematically depicted in Fig. S4. Two Pt wires served as contacts to the PANI sensor.

2.5. Photocatalytic reaction cell setup

In order to generate and indirectly detect ROS in the gas phase, a custom-made photocatalytic reaction cell with dimensions of L 7.0 cm × B 7.0 cm × H 4.0 cm was designed. A circular stage was mounted to a screw in the centre of the photocatalytic cell for height adjustment. All sidewalls of the cell are made of Plexiglas, while the cell lid is made of quartz glass for transmittance of UV light. The experimental setup is shown in Fig. 1.

The photocatalytic cell is directly connected to an in-house built gas mixer comprised of a series of flowmeters (Sho-Rate, Brooks Instrument) connected by copper tubes, a wetting stage and a drying stage with possibility to control the relative humidity of the compressed air. The different photocatalysts were placed on the circular stage, while two pieces of MB film were attached on the inner side of the quartz lid and work as ROS colourimetric indicators. The distance between the photocatalyst and the MB film could be adjusted in the range of 0.5–3 cm. A UV-LED light source with illumination intensity of 16 mW cm^{-2} and main peak at 365 nm (corresponds to a UV content of four suns illumination) was used to illuminate the photocatalyst from the top of the cell. By introducing a constant flow of air (14 mL min^{-1}) with 80%, 40% and 0% relative humidity (RH) into the reaction cell, hydroxyl radicals and other ROS are expected to be produced by the photocatalyst. It is also expected that the flow of air and convection will bring the photogenerated molecules towards the MB indicator. The UV–Vis spectra of the MB film were measured at several time intervals and the decolourisation percentage of MB film was calculated using Eq. (8).

$$\%\ \text{decolourization of MB film} = \left(1 - \frac{A_t}{A_0}\right) * 100 \quad (8)$$

where A_t is the absorbance after t min; A_0 is the absorbance at initial stage, i.e. $t = 0$ min. All experiments were conducted at room temperature.

2.6. Characterisation

The microstructures of the different TiO_2 NRs were investigated using an FEI Quanta 200 Field Emission Gun – Environmental SEM (FEG-ESEM). The crystal structure of the prepared TiO_2 NRs was characterised by X-ray diffraction (XRD). The XRD patterns were recorded in a DIFF5 instrument using CuKα-filtered radiation (λ = 1.5406 Å), where the diffractometer uses the Bragg-Brentano geometry in the range $2^\circ \leq 2\theta \leq 70^\circ$. The XRD diffraction data were analysed using DIFFRAC. EVA from Bruker, and the phase identification of crystalline materials was carried out by using the Crystallography Open Database (COD). The absorption spectrum of the MB dye embedded in Nafion® film was monitored with a UV–Vis spectrophotometer (SPECORD® 200 PLUS) over the wavelength range from 300 to 800 nm. Data analysis was carried out using the spectroanalytical software WinASPECT PLUS.

3. Results and discussion

3.1. Morphology, crystal structure and optical properties

SEM images of the four different samples used in this study are presented in Fig. 2.

It can be seen that after 2.5 h of hydrothermal process, the TiO_2 NRs are approx. 0.5 μm long with a diameter of 110 nm. When the hydrothermal process is extended to 4 h, the length and the diameter of both DP TiO_2 NRs and DP 1% N-TiO_2 NRs become approx. 2.3 μm and 270 nm, respectively. The nanoflower morphology shows somewhat larger nanorod diameter of around 400 nm. A summary of the obtained geometrical parameters is given in Table S1. Moreover, XRD confirmed the expected rutile crystal structure for all the prepared films (Fig. S5) [30].

3.2. Optical properties

It should be noted that the purpose of N-doping was to induce acceptor states near the valence band (VB) of TiO_2, therefore induce more holes [31]. It is expected that an isolated N 2p energy level above the O 2p VB will be formed, resulting in narrowed band gap, as well as an increased holes concentration (Fig. S6) [32,33]. As explained earlier, the main purpose is to design a device for the generation of ROS. This means that the photocatalyst can be confined inside the device and UVA radiation can be used to activate it. The use of diffuse reflectance spectroscopy (DRS) was mainly to indirectly confirm the content of N, which is expected to red shift the absorption edge of TiO_2 [33]. The diffuse reflectance spectra of the different TiO_2 NRs were fitted to an indirect band gap transition, and the results are displayed in Fig. 3.

Assuming that TiO_2 possesses an indirect transition and according to

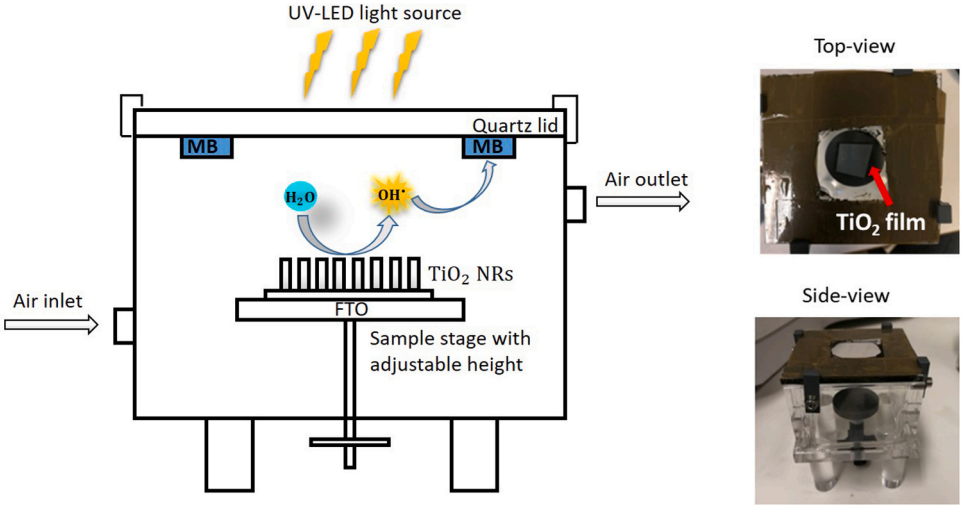

Fig. 1. Remote decolourisation of the MB film by UV/TiO_2 in the gas phase. (a) Shows a schematic of the photocatalytic cell with inlet and outlet for the supply humidified/dry air. The positioning of the MB colourimetric indicator at a distance from the photocatalyst is given. (b) Photographs of the gas phase photocatalytic reactor.

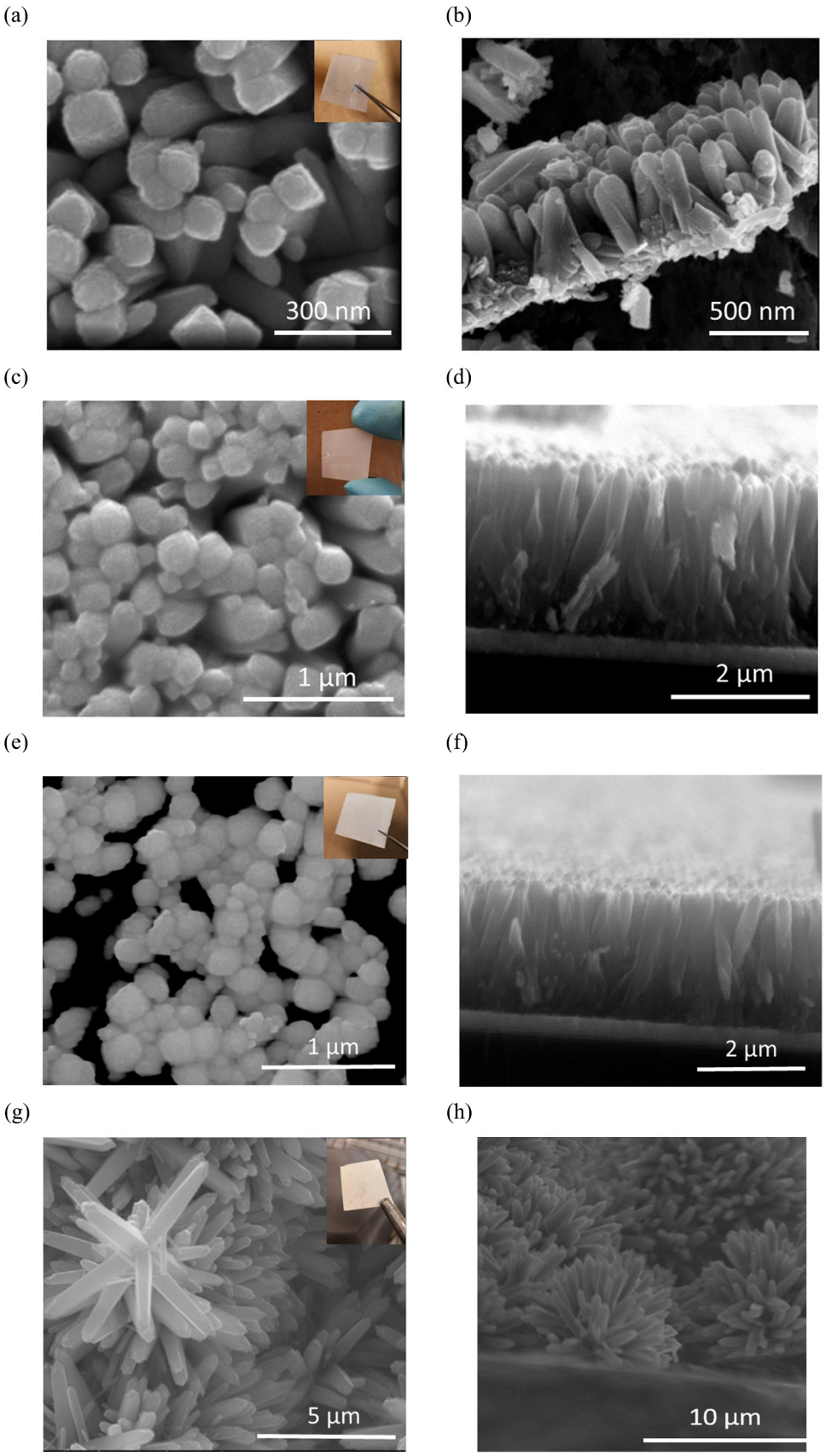

Fig. 2. Top view SEM images of the four different photocatalysts (left column) and their corresponding cross section view (right column). TiO_2 NRs on FTO at 150 °C after 2.5 h (a) and (b), DP TiO_2 NRs grown on FTO at 150 °C for 4 h (c) and (d), DP 1% N-TiO_2 NRs grown on FTO at 150 °C for 4 h (e) and (f), DP TiO_2 NFs on FTO at 150 °C for 4 h (g) and (h). The insets show photographs of the prepared films.

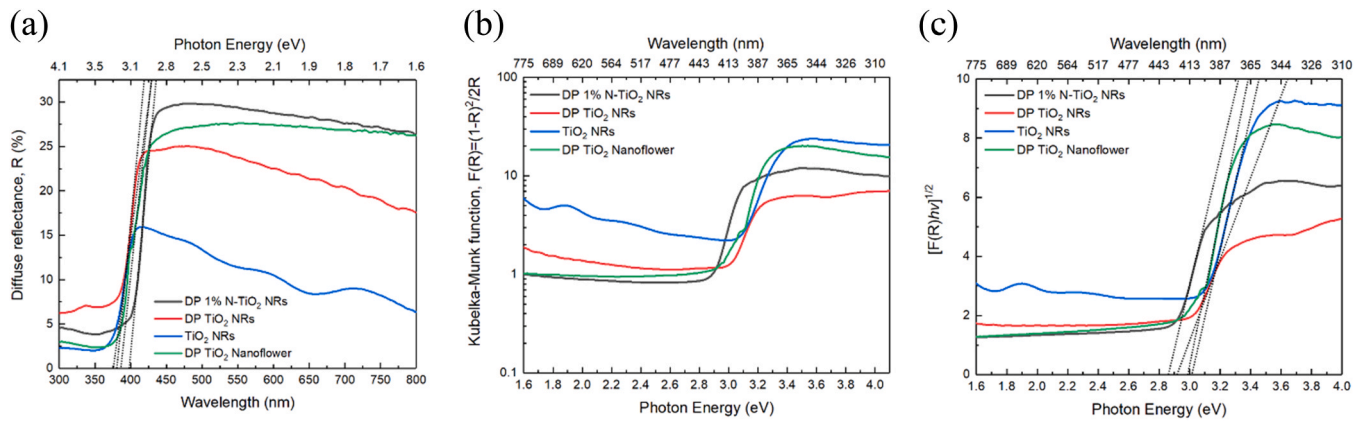

Fig. 3. Diffuse reflectance spectra without considering electronic transitions (a), Kubelka–Munk function (b), Tauc plot assuming indirect (allowed) transitions (c).

the Tauc plot in Fig. 3c, the samples DP TiO_2 NRs, TiO_2 NRs and DP TiO_2 NFs show corresponding band gaps of 2.93, 3.02 and 2.99 eV, respectively, which correspond well with the established bulk rutile TiO_2 band gap of 3.02 eV [34]. After the introduction of 1% N, the absorption edge shifted towards the lower energy region as expected, with a correspondingly narrower band gap of 2.88 eV, which implies the successful introduction of N in the lattice of TiO_2.

3.3. *Photocatalytic remote decolourisation of the MB indicator film*

Experiments were performed with only UVA illumination (blank experiments) and UVA plus the four photocatalysts. The distance between the surface of the photocatalyst and the MB film on the lid of the reaction cell was firstly set to 0.5 cm. The results of the remote photocatalytic decolourisation of the MB film are plotted as a function of the illumination time, as shown in Fig. 4a, c, e.

In most of the cases, the film decolourisation in the presence of the different TiO_2 NRs under UV illumination was enhanced compared to the blank experiments (purple line), except for the TiO_2 NRs sample, which has the shortest nanorods showing poor photocatalytic activity. The results indicate that both UVA illumination and an optimised photocatalyst were necessary for effective decomposition of the MB film. It is evident that the DP 1% N-TiO_2 NRs have the best photocatalytic activity under all RH conditions, further implying that the additional holes formed due to the introduction of N enhanced the performance of the material, therefore it can be assumed that more ROS were photogenerated. In all cases, the performance of the 1% N-doped sample is followed by the undoped DP TiO_2 NRs and then by the nanoflower morphology, while the TiO_2 NRs perform close to the background level, i.e. as with only UVA. It can be concluded that the aligned morphology outperforms the nanoflower morphology. Furthermore, the performance of the aligned morphology is increased by N-doping. It can also be seen that the 2 μm long nanorods perform better that the 0.5 μm ones, encouraging a future systematic study for the optimum length and packing density of the nanorods. The background decolourisation of the MB film is mostly related to the generation of ROS through the direct photolysis of water by the UVA illumination [35]. In addition, the reflected light reaching the MB indicator may also excite the dye, which is then oxidised in the absence of any reducing agent. The corresponding decolourisation efficiencies after 6 h of UV illumination are summarised in Table 2.

Similar experiments were carried out where the distance between the photocatalyst and the MB film on the lid of the reaction cell was increased to 3 cm. The results are presented in Fig. 4b, d, f. The decolourisation trend is similar to the previous case, but the efficiency was reduced significantly over the increased distance to the MB film. This is expected as the lifetimes of ROS range from microseconds to several seconds and even several minutes depending on the environment [36], with the lifetime of hydroxyl radicals being between tens and hundreds of milliseconds [37,38]. It is also interesting to note that the lifetime of singlet oxygen $^1O_2$ can be several tens of milliseconds in air [36,39], but their quantum yield and release in the air from a pure TiO_2 surface under UV illumination and an N-doped TiO_2 one under visible is 10^{-8} and 10^{-9}, respectively [40]. Hydroxyl radicals have a quantum yield of $5{\cdot}10^{-5}$ and a diffusion coefficient similar to that of water in air equal to $0.22{\cdot}10^{-4}\ m^2\ s^{-1}$ [40,41]. This puts it within the studied distances of 0.5 and 3 cm and the efficiency drop with increasing distance is reasonable. Therefore, we expect that the contribution of hydroxyl radicals is larger than that of singlet oxygen in the remote photodegradation of MB. On the other hand, it is well known that the superoxide anion radical and hydrogen peroxide have the longest lifetimes among the four major ROS so their contribution should be the largest. All in all, we believe that our approach to treat our data in terms of overall ROS activity for the remote degradation of MB is well justified.

The decolourisation percentages over the different photocatalysts of the MB film are summarised in Table 2. In general, a linear-dependent decolourisation was observed in most of the cases for all photocatalysts during the first measuring hour, when the degradation was measured every 10 min. An apparent lower degradation rate is observed when the measurements were taken only hourly.

Under the given experimental conditions, the best photocatalytic efficiency after 6 h of UV illumination was achieved with the 1% N-TiO_2 NRs at 80% RH at a distance of 0.5 cm, obtaining approx. 28% MB decolourisation. This is compared to the approx. 19% when the photocatalyst was placed farther (3 cm) from the indicator, also at 80% RH. Furthermore, approx. 6% decolourisation was achieved under UV illumination alone, 4% when the photocatalytic reaction occurred in the presence of the photocatalyst but in the dark, and 1.5% in the absence of both UV and the photocatalyst, i.e. only ambient illumination. These results are presented in Fig. 5.

Since 1% N-TiO_2 NRs showed the best photocatalytic efficiency, experiments in the presence of 1% N-TiO_2 NRs under the three relative humidity conditions were repeated five times for each condition, in order to check the reproducibility of the experimental results, and also to determine the standard deviation of the measurements. The results are given in Fig. S7 and summarised in Table S2.

Several observations may be rationalised by considering the role and properties of adsorbed water on the photocatalyst surface, as reactant for the formation of photogenerated $OH^{\bullet}$ radicals and by increased mobility in its liquid-like state at sufficient thickness appearing typically above 60% RH [42–44]. Firstly, one would expect that the lower RH conditions would eventually reach the level of decolourisation of the 80% RH, but this is not the case, showing the benefit of sufficient and liquid-like adsorbed water. Secondly, the lower efficiency with longer illumination intervals can be understood by heating of the catalyst and evaporation of the adsorbed water. In fact, the results can be best

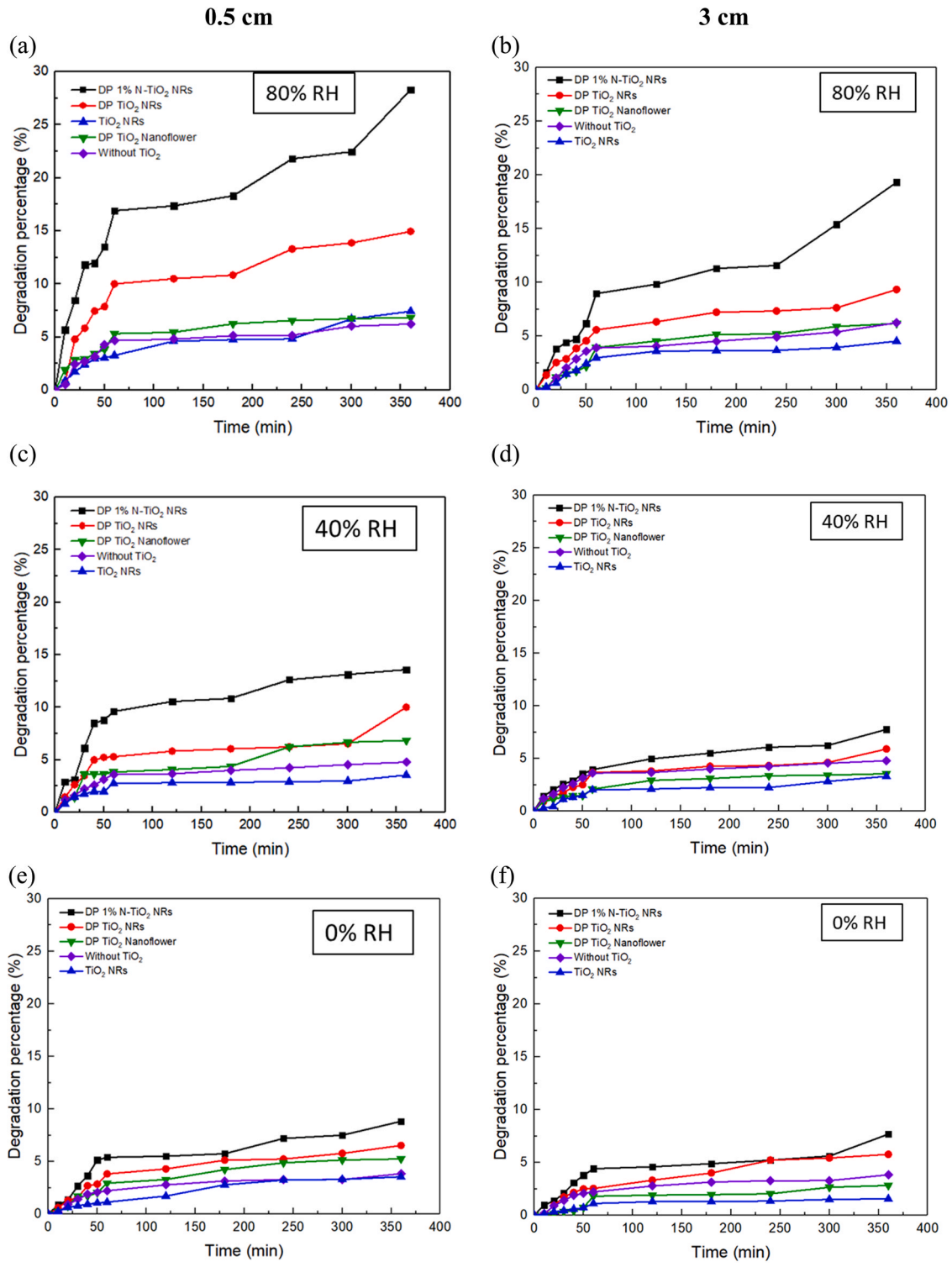

Fig. 4. Photocatalytic remote decolourisation of the MB film under 6 h UV illumination over the four morphologies of TiO_2 photocatalysts at (a) 80%, (b) 40% and (c) 0% RH. Distance between the NRs and the MB is 0.5 cm (left column) and 3 cm (right column). The y-axes are kept the same in order to highlight the differences.

understood by a finite amount of ROS generation for each dose of illumination between the interruption for MB decolouration measurements. After this dose, the water is desorbed and the catalyst is inactive. To validate this explanation, we repeated an experiment where we continued the sampling with a 10 min interval time beyond the 1 h mark (black, hollow squares in Fig. 5). In this case, it can be seen that the efficiency of the photocatalyst remains beyond 1 h mark and a 22% remote photocatalytic degradation of the film was achieved already after approx. 2 h at 10 min interval sampling time. This demonstrates the importance of the presence of a sufficiently thick layer of adsorbed water and hence the detrimental effect of the heat of the UV illumination source on the performance and efficacy of photocatalytic air cleaning devices.

Table 2
Decolourisation percentage of the MB film under UVA illumination for 6 h over the different morphologies of TiO_2 photocatalysts. Distance from the MB colourimetric indicator: 0.5 cm and 3 cm.

	Relative humidity (%)	DP 1% N-TiO_2 NRs (%)	DP TiO_2 NRs (%)	TiO_2 NRs (%)	DP TiO_2 NFs (%)	UVA alone (no photocatalyst) (%)
Distance 0.5 cm	80	28.3	15.0	7.4	7.0	6.3
	40	13.6	10.0	3.6	6.8	4.8
	0	8.9	6.5	3.5	5.1	3.8
Distance 3 cm	80	19.3	9.3	4.5	6.2	6.3
	40	7.8	5.9	3.3	3.5	4.8
	0	7.6	5.7	1.7	2.9	3.8

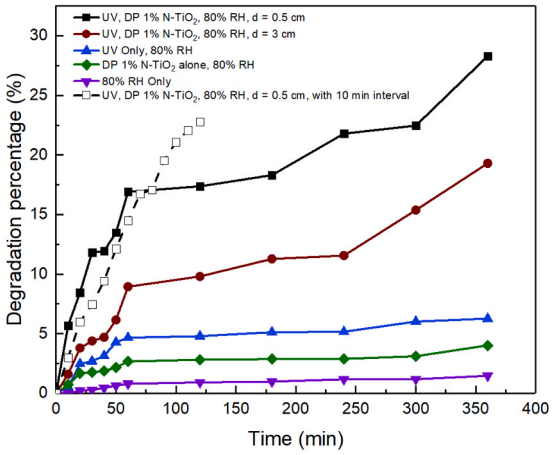

Fig. 5. Effect of UV light, photocatalyst and its placement on the photocatalytic decolourisation of MB film at 80% RH.

3.4. Photodecomposition kinetics of the MB colorimetric indicator

The influence of the RH level in the air stream on the remote photocatalytic decolourisation of the MB film was examined using the pseudo-first-order kinetics, which is usually applied to describe the degradation of most organic compounds [45,46]. The peculiarity of the present system is that the organic compound is not absorbed on the surface of the photocatalyst but is degraded at a distance. For these reasons, the MB film decolourisation rate was calculated using Eq. (9), where k is first-order of the decolourisation rate [47].

$$r_0 = -\frac{dC}{dt} = kC \quad (9)$$

It should be mentioned that we did not perform a calibration curve of dried MB films in Nafion® as we wanted to look into the absolute degradation efficiency of our system. The concentration of such dyes is directly proportional to the absorption intensity (ABS), therefore and in order to find the absolute degradation rate, C is replaced by ABS. Therefore, by integrating the input (ABS_0) and output (ABS) concentration limits, the equation can be simplified to Eq. (10):

$$\ln\left(\frac{ABS_0}{ABS}\right) = kt \quad (10)$$

The experimental data obtained during the first hour were used for the calculations of the reaction rate, in order to avoid variation due to the competitive effects of the intermediate products [48].

The concentration of MB as a function of illumination time under various RH is shown in Fig. 6a. The highest decolourisation rate was obtained at 80% RH, and the corresponding first order kinetic curves, which show a linear relationship, are presented in Fig. 6b. The decolourisation rate was estimated from the slope of each straight line. The R^2 shows that the first-order kinetic model represents well the system of photodecomposition reaction of the MB film at a proximity from the illuminated TiO_2 surface [47,49]. A more extended comparison of the kinetics and their corresponding decolourisation rates for the four photocatalysts at the three RH are provided in Table S3. The obtained decolourisation rates of the DP 1% N-TiO_2 NRs, DP TiO_2 NRs, DP TiO_2 NFs and TiO_2 NRs were 3.2, 1.9, 0.9 and 0.6 10^{-3} min^{-1} (Fig. S8), respectively, which clearly show that the fastest decolourisation rate was obtained with the N-doped sample.

3.5. Polyaniline (PANI) sensor on interdigitated electrode (IDE) for hydroxyl radicals detection

The PANI film was electrodeposited on the IDE using the pulse electrodeposition described in the experimental section. The surface morphology of PANI prepared on IDEs is displayed in Fig. S9, where it can be seen that the IDEs is completely covered by the PANI film. In this setup, the PANI sensor [25,26] was placed in the same position as the MB film, as depicted in Fig. 1, and the active sensing area was 0.38 cm^2.

Initially, we tested the PANI sensor with the Fenton reaction as described by Fang et al. [26] and we found their results reproducible. The change in the conductivity of the sensor over time is presented in Fig. S10. After testing with the Fenton reaction, the film was destroyed

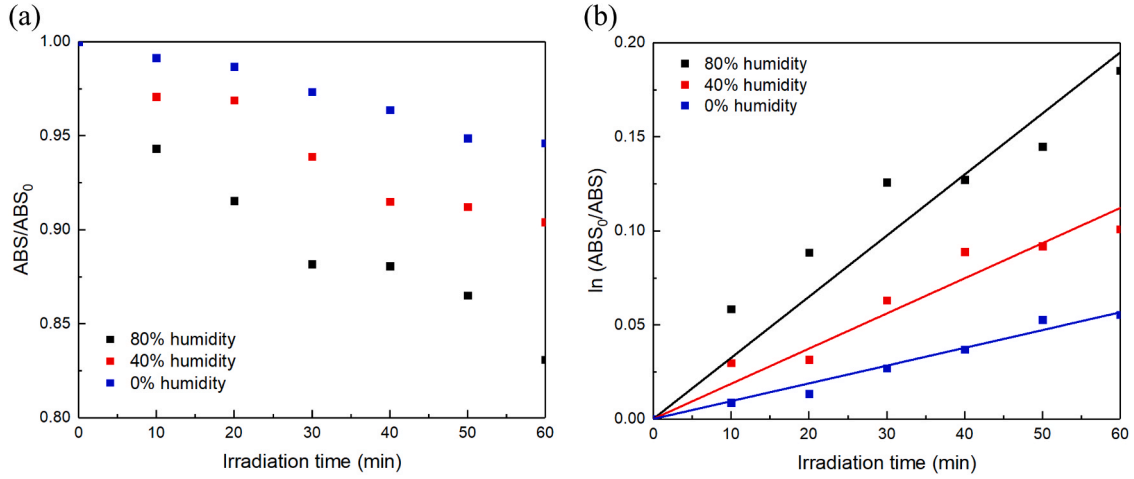

Fig. 6. ABS/ABS_0 ratio at 0%, 40% and 80% RH (a), first order kinetics plot for the photocatalytic decolourisation of MB film over 1% N-TiO_2 NRs under UV illumination with the relative humidity. R^2 at 80%, 40%, 0% RH were 0.975, 0.984 and 0.992 respectively (b).

as the concentration of hydroxyl radicals is expected to be of the order of mM (see photograph in Fig. S11). Subsequently, conductivity measurements were performed using PANI coated on IDEs as hydroxyl radicals sensor in the same photocatalytic reactor as with the MB film under the best conditions, i.e. DP 1% N-TiO_2 NRs as the photocatalyst at 80% RH. In this case, we assume that the selectivity towards hydroxyl radicals is greater than in the photodegradation of MB, therefore our analysis refers explicitly to them. Blank experiments in the presence of the photocatalyst alone, and in the presence of UVA alone, were included as the background signal of the sensor. All conductivity measurements were performed using the same PANI sensor, so that the initial current was the same. The results are presented in Fig. 7, where the change in current of the PANI sensor was plotted as arbitrary unit for better visualisation.

In the presence of photocatalyst alone (blue curve), the baseline current of the PANI sensor did not change during 2 h of operation (198.4–198.5 μA). This result excludes the possibility that the photocatalyst alone could interact with PANI. In the presence of UVA alone (red curve), some current decrease (0.3 μA) was observed when light was switched on and off (198.4–198.1 μA). This can be attributed to the radicals produced by the direct photolysis of water vapour, a finding that correlates well with the remote degradation of the MB film in the presence of UVA alone (Fig. 5). In the presence of both photocatalyst and UVA illumination, the current of the PANI decreased further (198.4–197.7 μA) compared to the blank ones during the first 15 min of UV light on (from 1400 to 2300 s), which then remained constant throughout the rest of the experiment, suggesting the background $OH^{\bullet}$ generation rate due to the UVA illumination alone. This correlates well with the depletion of the water layer on the surface of the oxide due to the heat from the constant illumination. After the critical dose of illumination is reached the photocatalyst is inactive and the background generation of $OH^{\bullet}$ stabilises the current of the sensor at its lowest point. When the UVA was switched off, the catalyst surface cool down again, and the liquid-like water layer is regenerated. Consequently, the current increased again close to its initial value (black curve). This behaviour was further confirmed by extending the reaction time to 5 h, as seen in Fig. S12, emphasising the major role of sufficient thickness of the adsorbed water layer. All in all, the PANI sensor coated on IDEs showed good response and reproducibility during the process. As also expected, the concentration of $OH^{\bullet}$ generated from the gas-phase photocatalytic reaction was much lower than that of the liquid-phase Fenton reaction. Consequently, the PANI sensor was not damaged. The results demonstrated great potential of the PANI sensor for application in real-time detection of photogenerated $OH^{\bullet}$.

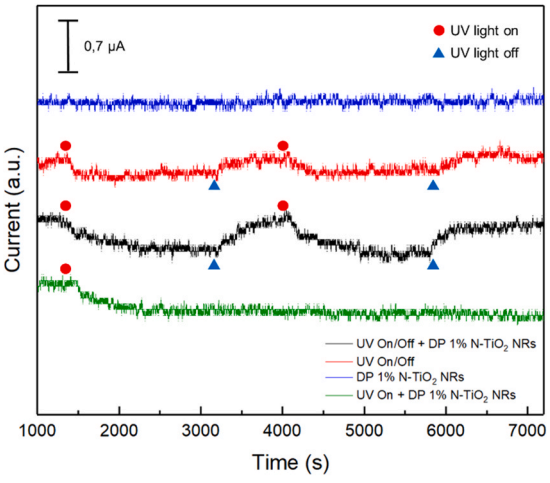

Fig. 7. Change in current of PANI on IDEs for the online detection of $OH^{\bullet}$ in the presence of DP 1% N-TiO_2 NRs at 80% RH, under applied voltage of 0.01 V and a sample period of 0.5 s for 2 h plotted as an arbitrary unit for better visualisation.

Furthermore, we attempted a rough calculation of the amount of $OH^{\bullet}$ radicals produced by the TiO_2 NRs based on the results of Fig. 7. From the integration between a light on/off cycle the electric charge can be found, and assuming a one electron reaction, the amount of $OH^{\bullet}$ reaching the surface of the PANI sensor was estimated to be approx. $3 \cdot 10^{15}$ molecules after 2700 s. The corresponding production rate was approx. $1.2 \cdot 10^{12}$ molecules s^{-1} per 0.38 cm^2 sensing area (calculations are provided in the SI and Fig. S13). The distance of the photocatalyst from the PANI sensor was 0.5 cm, therefore the amount can be rearranged to $1.2 \cdot 10^{12}$ molecules s^{-1} per 0.19 cm^3. This amount of hydroxyl radicals correlates very well with the findings of Murakami et al., where they reported $5.0 \cdot 10^{12}$ molecules cm^{-3} [41].

4. Conclusions

In this work, a gas-phase custom-designed photocatalytic reactor was built in order to probe the photogeneration of ROS, and determine the effect of RH, light and distance in the remote decolourisation of a colourimetric indicator. Four different morphologies of TiO_2 nanorods were assessed as potential photocatalysts, and our results indicate that the N-doped TiO_2 nanorods showed the best performance in the remote photocatalytic degradation of the MB dye embedded in Nafion®. The main reason is related to the higher concentration of holes as a result of N doping. The doped material exhibited a 26% decolourisation of the indicator and a pseudo first-order decolourisation rate of $3.2 \cdot 10^{-3}$ min^{-1} at a distance of 0.5 cm, under air stream of 80% RH and 16 mW cm^{-2} UVA illumination. At a distance of 3 cm from the indicator, the efficiency was reduced to 19%, which nevertheless demonstrates the ability of ROS to survive a considerable distance from the photocatalyst surface.

A principal finding from this work is the major role adsorbed water in sufficient thickness plays as reactant for generation of hydroxyl radicals. This means that the photocatalyst has to be kept cold permanently or cooled intermittently. This can be done by moderating the illumination by power regulation or chopping or by longer on/off cycles – in our case through intervention for external analysis of MB decolourisation. Operando techniques, such as FT-IR could further elucidate the changes in the adsorbed water layers while the temperature on the surface of the oxide varies under certain light/dark cycles. Probing the temperature of the oxide surface is also of great value.

Finally, we were able to estimate *in*-situ the amount of hydroxyl radicals produced by a simple electrochemical sensor based on PANI. Our results suggest that approx. $1.2 \cdot 10^{12}$ molecules s^{-1} per 0.38 cm^2 sensing area were photocatalytically produced. Laser-induced fluorescence (LIF) spectroscopy has a detection limit of 10^6 molecules [37,50] and our results suggest that LIF could be a suitable and direct hydroxyl radicals detection method in the gas phase that could be combined with the present photocatalytic reactor. Nevertheless, previously reported amounts of hydroxyl radicals measured by LIF show excellent correlation with the ones reported by the PANI sensor, making the latter a good, inexpensive and simple detection alternative.

The proposed gas-phase photocatalytic ROS generation-detection system demonstrates a promising route for fundamental understanding and development of efficient and controllable air cleaning/purification/disinfection devices.

CRediT authorship contribution statement

Xinwei Sun: Investigation, Visualization, Writing - original draft, Writing - review & editing. **Kaiqi Xu:** Investigation, Methodology, Validation, Writing - review & editing. **Athanasios Chatzitakis:** Conceptualization, Methodology, Supervision, Validation, Writing - original draft, Writing - review & editing. **Truls Norby:** Conceptualization, Methodology, Supervision, Validation, Writing - original draft, Writing - review & editing.

Declaration of Competing Interest

The authors declare that they have no known competing financial interests or personal relationships that could have appeared to influence the work reported in this paper.

Appendix A. Supporting information

Supplementary data associated with this article can be found in the online version at doi:10.1016/j.jece.2020.104809.

References

[1] S.-S. Kim, D.-H. Kang, D.-H. Choi, M.-S. Yeo, K.-W. Kim, Comparison of strategies to improve indoor air quality at the pre-occupancy stage in new apartment buildings, Build. Environ. 43 (2008) 320–328.

[2] S.W. Verbruggen, TiO2 photocatalysis for the degradation of pollutants in gas phase: from morphological design to plasmonic enhancement, J. Photochem. Photobiol. C Photochem. Rev. 24 (2015) 64–82.

[3] N.E. Klepeis, W.C. Nelson, W.R. Ott, J.P. Robinson, A.M. Tsang, P. Switzer, J. V. Behar, S.C. Hern, W.H. Engelmann, The National Human Activity Pattern Survey (NHAPS): a resource for assessing exposure to environmental pollutants, J. Expo. Sci. Environ. Epidemiol. 11 (2001) 231–252.

[4] L. Zhong, F. Haghighat, Photocatalytic air cleaners and materials technologies – abilities and limitations, Build. Environ. 91 (2015) 191–203.

[5] S. Wang, H.M. Ang, M.O. Tade, Volatile organic compounds in indoor environment and photocatalytic oxidation: State of the art, Environ. Int. 33 (2007) 694–705.

[6] A.H. Mamaghani, F. Haghighat, C.-S. Lee, Photocatalytic oxidation technology for indoor environment air purification: the state-of-the-art, Appl. Catal. B Environ. 203 (2017) 247–269.

[7] J. Yang, D. Li, Z. Zhang, Q. Li, H. Wang, A study of the photocatalytic oxidation of formaldehyde on Pt/Fe2O3/TiO2, J. Photochem. Photobiol. A Chem. 137 (2000) 197–202.

[8] J. Zhao, X.D. Yang, Photocatalytic oxidation for indoor air purification: a literature review, Build. Environ. 38 (2003) 645–654.

[9] D. Blake, Bibliography of Work on the Heterogeneous Photocatalytic Removal of Hazardous Compounds from Water and Air, National Renewable Energy Lab., Golden, CO (US), Technical Report, 2001.

[10] R. Andreozzi, V. Caprio, A. Insola, R. Marotta, Advanced oxidation processes (AOP) for water purification and recovery, Catal. Today 53 (1999) 51–59.

[11] J. Blanco, S. Malato, Solar Detoxification, UNESCO Publishing, 2003.

[12] S. Malato, P. Fernández-Ibáñez, M.I. Maldonado, J. Blanco, W. Gernjak, Decontamination and disinfection of water by solar photocatalysis: recent overview and trends, Catal. Today 147 (2009) 1–59.

[13] C. Comninellis, A. Kapalka, S. Malato, A. Parsons Simon, I. Poulios, D. Mantzavinos, Advanced oxidation processes for water treatment: advances and trends for R&D, J. Chem. Technol. Biotechnol. 83 (2008) 769–776.

[14] E. Bizani, K. Fytianos, I. Poulios, V. Tsiridis, Photocatalytic decolorization and degradation of dye solutions and wastewaters in the presence of titanium dioxide, J. Hazard. Mater. 136 (2006) 85–94.

[15] F. Khodadadian, M.W. de Boer, A. Poursaeidesfahani, J.R. van Ommen, A. I. Stankiewicz, R. Lakerveld, Design, characterization and model validation of a LED-based photocatalytic reactor for gas phase applications, Chem. Eng. J. 333 (2018) 456–466.

[16] H. Einaga, S. Futamura, T. Ibusuki, Heterogeneous photocatalytic oxidation of benzene, toluene, cyclohexene and cyclohexane in humidified air: comparison of decomposition behavior on photoirradiated TiO2 catalyst, Appl. Catal. B Environ. 38 (2002) 215–225.

[17] G. Vincent, P.M. Marquaire, O. Zahraa, Photocatalytic degradation of gaseous 1-propanol using an annular reactor: kinetic modelling and pathways, J. Hazard. Mater. 161 (2009) 1173–1181.

[18] N. Bouazza, M.A. Lillo-Ródenas, A. Linares-Solano, Photocatalytic activity of TiO2-based materials for the oxidation of propene and benzene at low concentration in presence of humidity, Appl. Catal. B Environ. 84 (2008) 691–698.

[19] A.K. Boulamanti, C.J. Philippopoulos, Photocatalytic degradation of C5–C7 alkanes in the gas–phase, Atmos. Environ. 43 (2009) 3168–3174.

[20] M. Sleiman, P. Conchon, C. Ferronato, J.-M. Chovelon, Photocatalytic oxidation of toluene at indoor air levels (ppbv): towards a better assessment of conversion, reaction intermediates and mineralization, Appl. Catal. B Environ. 86 (2009) 159–165.

[21] W. Wang, Y. Ku, Photocatalytic degradation of gaseous benzene in air streams by using an optical fiber photoreactor, J. Photochem. Photobiol. A Chem. 159 (2003) 47–59.

[22] E. Piera, J.A. Ayllón, X. Doménech, J. Peral, TiO2 deactivation during gas-phase photocatalytic oxidation of ethanol, Catal. Today 76 (2002) 259–270.

[23] ODOROX, Hydroxyl Generators, 2018.

[24] S. Gligorovski, R. Strekowski, S. Barbati, D. Vione, Environmental implications of hydroxyl radicals ((*)OH, Chem. Rev. 115 (2015) 13051–13092.

[25] J.-Y. Fang, K.C. Fang, C.-P. Hsu, C.H. Chu, J. Liu, Y.-L. Wang, Investigation of the hydroxyl radical sensor with conductance change of polyaniline, ECS Trans. 64 (2014) 63–67.

[26] K.-C. Fang, C.-P. Hsu, Y.-W. Kang, J.-Y. Fang, C.-C. Huang, C.-H. Hsu, Y.-F. Huang, C.-C. Chen, S.-S. Li, J. Andrew Yeh, D.-J. Yao, Y.-L. Wang, Realization of an ultra-sensitive hydrogen peroxide sensor with conductance change of horseradish peroxidase-immobilized polyaniline and investigation of the sensing mechanism, Biosens. Bioelectron. 55 (2014) 294–300.

[27] B. Liu, E.S. Aydil, Growth of oriented single-crystalline rutile TiO2 nanorods on transparent conducting substrates for dye-sensitized solar cells, J. Am. Chem. Soc. 131 (2009) 3985–3990.

[28] H.-F. Jiang, X.-X. Liu, One-dimensional growth and electrochemical properties of polyaniline deposited by a pulse potentiostatic method, Electrochim. Acta 55 (2010) 7175–7181.

[29] V. Tsakova, A. Milchev, J.W. Schultze, Growth of polyaniline films under pulse potentiostatic conditions, J. Electroanal. Chem. 346 (1993) 85–97.

[30] M. Grandcolas, B. Wabende, J. Yang, S. Mei, K. Xu, T. Norby, A. Chatzitakis, Preparation of TiO2 rutile nanorods decorated with cobalt oxide nanoparticles for solar photoelectrochemical activity, Mater. Lett. 247 (2019) 1–3.

[31] Z. Shayegan, C.-S. Lee, F. Haghighat, TiO2 photocatalyst for removal of volatile organic compounds in gas phase – a review, Chem. Eng. J. 334 (2018) 2408–2439.

[32] R. Asahi, T. Morikawa, T. Ohwaki, K. Aoki, Y. Taga, Visible-light photocatalysis in nitrogen-doped titanium oxides, Science 293 (2001) 269–271.

[33] H. Irie, Y. Watanabe, K. Hashimoto, Nitrogen-concentration dependence on photocatalytic activity of TiO2-xNx powders, J. Phys. Chem. B 107 (2003) 5483–5486.

[34] L. Zhang, H.H. Mohamed, R. Dillert, D. Bahnemann, Kinetics and mechanisms of charge transfer processes in photocatalytic systems: a review, J. Photochem. Photobiol. C Photochem. Rev. 13 (2012) 263–276.

[35] S. Parsons, Advanced Oxidation Processes for Water and Wastewater Treatment, IWA Publishing, 2004.

[36] Y. Nosaka, A.Y. Nosaka, Generation and detection of reactive oxygen species in photocatalysis, Chem. Rev. 117 (2017) 11302–11336.

[37] D.E. Heard, M.J. Pilling, Measurement of OH and HO2 in the troposphere, Chem. Rev. 103 (2003) 5163–5198.

[38] Y. Sadanaga, A. Yoshino, K. Watanabe, A. Yoshioka, Y. Wakazono, Y. Kanaya, Y. Kajii, Development of a measurement system of OH reactivity in the atmosphere by using a laser-induced pump and probe technique, Rev. Sci. Instrum. 75 (2004) 2648–2655.

[39] T. Daimon, Y. Nosaka, Formation and behavior of singlet molecular oxygen in TiO2 photocatalysis studied by detection of near-infrared phosphorescence, J. Phys. Chem. C 111 (2007) 4420–4424.

[40] K. Naito, T. Tachikawa, M. Fujitsuka, T. Majima, Real-time single-molecule imaging of the spatial and temporal distribution of reactive oxygen species with fluorescent probes: applications to TiO2 photocatalysts, J. Phys. Chem. C 112 (2008) 1048–1059.

[41] Y. Murakami, K. Endo, I. Ohta, A.Y. Nosaka, Y. Nosaka, Can OH radicals diffuse from the UV-irradiated photocatalytic TiO2 surfaces? Laser-induced-fluorescence study, J. Phys. Chem. C 111 (2007) 11339–11346.

[42] K. Xu, A. Chatzitakis, E. Vøllestad, Q. Ruan, J. Tang, T. Norby, Hydrogen from wet air and sunlight in a tandem photoelectrochemical cell, Int. J. Hydrog. Energy 44 (2019) 587–593.

[43] S.Ø. Stub, E. Vøllestad, T. Norby, Mechanisms of protonic surface transport in porous oxides: example of YSZ, J. Phys. Chem. C 121 (2017) 12817–12825.

[44] S.Ø. Stub, K. Thorshaug, P.M. Rørvik, T. Norby, E. Vøllestad, The influence of acceptor and donor doping on the protonic surface conduction of TiO 2, Phys. Chem. Chem. Phys. 20 (2018) 15653–15660.

[45] J. Cunningham, G. Al-Sayyed, S. Srijaranai, Adsorption of model pollutants onto TiO2 particles in relation to photoremedation of contaminated water, in: G. Helz, R. Zepp, D. rosby (Eds.), Aquatic and Surface Photochemistry, CRC Press, Boca Raton, FL, 1994, pp. 317–348 (Chapter 322).

[46] C. Yang, W. Dong, G. Cui, Y. Zhao, X. Shi, X. Xia, B. Tang, W. Wang, Highly-efficient photocatalytic degradation of methylene blue by PoPD-modified TiO 2 nanocomposites due to photosensitization-synergetic effect of TiO2 with PoPD, Sci. Rep. 7 (2017) 3973.

[47] K. Hayat, M.A. Gondal, M.M. Khaled, Z.H. Yamani, S. Ahmed, Laser induced photocatalytic degradation of hazardous dye (Safranin-O) using self synthesized nanocrystalline WO3, J. Hazard. Mater. 186 (2011) 1226–1233.

[48] A. Chatzitakis, C. Berberidou, I. Paspaltsis, G. Kyriakou, T. Sklaviadis, I. Poulios, Photocatalytic degradation and drug activity reduction of Chloramphenicol, Water Res. 42 (2008) 386–394.

[49] N. Daneshvar, D. Salari, A.R. Khataee, Photocatalytic degradation of azo dye acid red 14 in water on ZnO as an alternative catalyst to TiO2, J. Photochem. Photobiol. A Chem. 162 (2004) 317–322.

[50] Y. Matsumi, M. Kono, T. Ichikawa, K. Takahashi, Y. Kondo, Laser-induced fluorescence instrument for the detection of tropospheric OH radicals, Bull. Chem. Soc. Jpn. 75 (2002) 711–717.